This document is the accepted manuscript version of the following article:

Hosseini, E., Robmann, S., Lüthi, T., Affolter, C., & Mazza, E. (2022). Tensile response characterization and constitutive modeling of LPBF Ti6Al4V thin struts. Advanced Engineering Materials. https://doi.org/10.1002/adem.202201135

# Tensile Response Characterization and Constitutive Modelling of LPBF Ti6Al4V Thin Struts

Ehsan Hosseini[a,*], Serjosha Robmann[a,b], Thomas Lüthi[a], Christian Affolter[a], Edoardo Mazza[a,b]

[a] *Empa Swiss Federal Laboratories for Materials Science & Technology, Dübendorf, Switzerland*
[b] *ETH Zurich, Department of Mechanical and Process Engineering, Institute for Mechanical Systems, Zürich, Switzerland*

**Abstract**

Additive manufacturing enables the fabrication of orthopaedic implants with lattice materials whose topology is (locally) tailored to mimic the mechanical response of native bone. Detailed analysis of such lattice structures for optimizing their mechanical biocompatibility requires an understanding of the mechanical response of their constituent components, i.e. 'struts'. The present study conducted a series of miniature-specimen mechanical experiments to analyse the apparent stress-strain response of AM Ti6Al4V struts with nominal gauge diameters of 200 µm, 300 µm, 400 µm and 500 µm, manufactured through the laser powder bed fusion process under four different build orientations. The 'true' geometries of the struts were then derived based on observations from micro-computed tomography (µCT) to discuss the size- and orientation-dependence of the 'geometrical mismatch' as well as the 'true' stress-strain response of the struts. It is however argued that considering the 'true' mechanical response of struts in the design and topology optimization of lattice-based implants is not practically feasible, since it requires information regarding the 'true' geometry of each strut within the implant that is not accessible at the design stage. As an alternative, consideration of a representative 'apparent' constitutive model in finite element simulations representing the 'nominal' geometry of the lattices provides acceptable approximations of their experimentally observed mechanical response and, therefore might be employed for design analysis and topology optimization of lattice-based implants.

*Keywords:* Miniaturised mechanical experiment, Additive manufacturing, Constitutive modeling, FE analysis, Ti6Al4V lattices

## 1. Introduction

Orthopaedic surgeries (including joint replacements) and the demand for orthopaedic implants have increased rapidly in the past few decades due to the increasing number of sports-related injuries as well as the increase in the average life spans and physical activity among the elderly [1, 2]. Metals are the common choice for load-bearing implants due to their high mechanical strength and fracture toughness [3]. Stainless steel, Co-Cr and titanium alloys are the most widely used metallic implant materials with elastic moduli of ~180 GPa, 210 GPa and 100 GPa, respectively [4]. These values are much higher than elastic moduli of the trabecular (~2 GPa [5]) and cortical bone (ranging from 10 GPa to 30 GPa [6–8]) and therefore induce a high risk of the so-called stress shielding effect [9]; i.e. the stiffness mismatch between the implant and the surrounding bone reduces the normal physiological load of the bone and leads to bone resorption and weaking of the surrounding bone tissue, and ultimately, implant loosening and the need for complex revision surgeries [4, 10–13]. Porous implants have been widely acknowledged as a solution to avoid stress shielding due to their reduced stiffness [14]. Furthermore, porous structures might provide channels for neovascularization and accelerate the process of osseointegration [15].

Conventional techniques for manufacturing porous metallic structures, such as space holder technology [16, 17], do not control the subtle internal structure leading to undesired pore distribution and consequently unbalanced stress distribution and a high risk of implant failure [18]. Furthermore, not all pores may be interconnected, resulting in the existence of the so-called blind alleys, which inhibit effective integration of native bone [18, 19].

The rapidly developing additive manufacturing (AM) technology is currently being considered for the fabrication of Ti6Al4V implants with internal periodic architecture, known as lattice structures [20–22]. The two common AM techniques for the fabrication of lattice structures are laser powder bed fusion (LPBF) and electron beam melting (EBM) [21, 23]. Lattice structures potentially fulfill both mechanical and biological requirements of prosthetic devices, led to consider them as an alternative to bulk metals for the next generation of orthopaedic implants [24, 25]. The main advantage of AM over the conventional manufacturing methods is the ability to manufacture implants with interconnected pores of controlled size and shape [18]. The implant topology (e.g. lattice type, strut thickness, porosity) can be locally tailored to mimic mechanical properties of the native bone and therefore avoid stress-shielding [18]. Additionally, AM allows design customization of implants in order to match the specific patient anatomical requirements [26]. Furthermore, the interconnected network of pores and the rough surface of AM lattices promote osseointegration

*Corresponding author: E. Hosseini, ehsan.hosseini@empa.ch, Empa Swiss Federal Laboratories for Materials Science & Technology

and bone ingrowth [24, 24, 27, 28].

The mechanical behavior of lattice structures is still far from being fully understood [24, 29–32]. On the other hand, design of implant systems with desired deformation response requires the adoption of reliable mechanical analysis solutions for AM lattice structures in topology optimization routines [33]. To this end, analysis of lattice structures requires an understanding of the stress-strain response of their constituent components called 'struts'. Several studies have investigated the relationship between manufacturing parameters and the mechanical properties of lattice materials. However, little research focus has been on evaluating the mechanical response of struts; examples are the work of Murchio et al. [24], Perez et al. [34], Pehlivan et al. [35] and Weissmann et al. [36] who elevated the mechanical response of AM struts made of Ni- and Ti-base alloys, but often for strut diameters larger than those typically adopted for lattice implants.

Therefore, this study presents the outcomes of a comprehensive experimental program aiming at characterizing the tensile deformation response of miniature LPBF Ti6Al4V specimens with gauge length of 1 mm and (nominal) diameters of 200 µm, 300 µm, 400 µm and 500 µm, representing individual struts within implant lattices. To quantify the anisotropy in the mechanical response of the struts, the testpieces were manufactured under four different build orientations. Six uniaxial tensile experiments were performed for each diameter-orientation class to capture the variability of their mechanical response, leading to a total of 96 conducted miniature experiments. These observations were analysed to derive apparent constitutive models for each class of samples.

It is well-known that the manufactured dimensions of AM builds might not accurately match the designed geometries, in particular for small-size structures [37, 38]. Micro-computed tomography (µCT) was therefore employed to determine the 'true' geometry of the built miniature samples and accordingly discuss the size- and orientation-dependence of their 'geometrical mismatch' as well as their 'true' stress-strain response, i.e. based on the real geometry of the samples.

Finally, it is argued that considering the 'true' mechanical response of struts in the design and topology optimization analyses of lattice-based implants is not practically feasible, since it requires information regarding the 'true' geometry of each strut within the implant that is not accessible at the design stage. As an alternative, this study evaluated the reliability of considering the apparent constitutive response of the struts in finite element (FE) models representing the 'nominal' topology of lattices. Comparison of the outcomes of such FE analysis with the experimental observations from tensile testing of tetrahedron lattice-based samples with nominal strut diameter of 200 µm indicated an acceptable level of accuracy which justifies the adoption of such approximate analysis strategy for design and topology optimization purposes.

## 2. Materials and Methods

This section describes the procedure for the fabrication of the testpieces, mechanical experiments, µCT assessment and details of the performed FE analyses.

Table 1: Chemical Composition (mass %) for the employed Ti6Al4V powder.

| Al | V | Fe | O | C | N | H | Ti |
|---|---|---|---|---|---|---|---|
| 5.5-6.5 | 3.5-4.5 | ≤0.25 | ≤0.13 | ≤0.08 | ≤0.05 | ≤0.01 | Bal. |

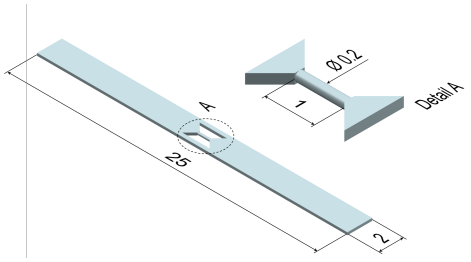


Figure 1: Nominal geometry for the LPBF manufactured Ti6Al4V miniature tensile testpieces with $d_{nom}$ = 200 µm (dimensions are in mm).

### 2.1. Fabrication of testpieces

The examined testpieces were manufactured via LPBF (Renishaw AM–400) using a 200 W laser with an energy density of 83 J mm$^{-3}$ and a spot diameter of 70 µm. The chemical composition of the Ti6Al4V powder is given in Table 1. The size of powder particles was 14 µm to 45 µm, and a layer thickness of 30 µm was used for fabricating the testpieces. The build chamber was flushed with argon before starting the LPBF process to minimise the risk of Ti6Al4V powder contamination. After fabrication, the testpieces were annealed at (850 ± 10) °C for two hours. No post-process surface or hot isostatic pressing (HIP) treatment was performed. Following the heat treatment, the specimens were removed from the build plate with electrical discharge machining (EDM).

Fig. 1 shows an example of the designed geometries for the miniature tensile specimens. The samples were manufactured with a gauge length of 1 mm, with four nominal diameters ($d_{nom}$) of 200 µm, 300 µm, 400 µm and 500 µm and under four build orientations ($\alpha$) of 0°, 30°, 60° and 90° ($\alpha$: the angle between sample axis and build plate). Each sample included one central and two lateral struts. The two lateral struts were cut before the tensile testing.

Additionally, tetrahedron lattice-based tensile specimens with 6×6×6 unit cells were manufactured under the same LPBF processing conditions, see Fig. 2. The tetrahedron topology of the lattices had the following characteristics: nominal cell size = 1200 µm, pore size = 500 µm, strut diameter = 200 µm, and porosity = 75 %. The adopted lattice topology from [27, 38] is suitable for load-bearing orthopaedic implants and satisfies the bone ingrowth requirements as well as the LPBF process constraints.

### 2.2. Mechanical experiments

A servo-hydraulic MTS machine (MTS Systems Corporation, Eden Prairie, USA), mounted horizontally on an anti-vibration table, was used for examining the tensile response of the LPBF Ti6Al4V miniature-specimens, Fig. 3a. Depending

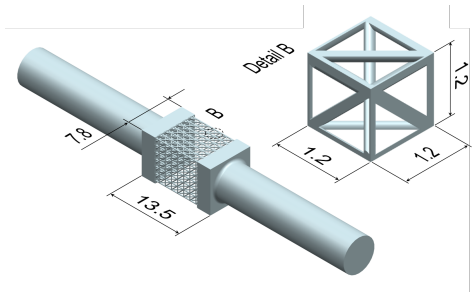


Figure 2: Nominal geometry for the LPBF manufactured Ti6Al4V tetrahedron-based lattice specimens (dimensions are in mm).

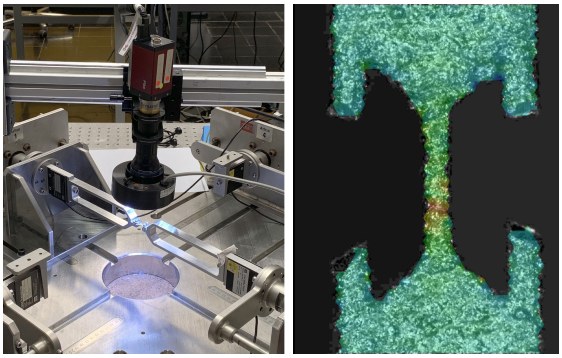

(a)

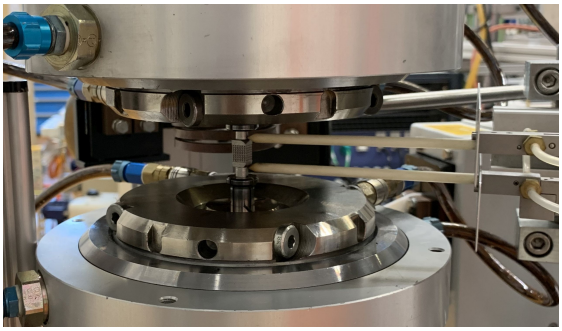

(b)

Figure 3: The employed experimental setup for tensile testing of a) miniature, and b) lattice specimens.

on the expected maximum force for each experiment, a load cell with a capacity of 100 N or 2500 N was used. The tensile tests were conducted at a cross-head speed equivalent to the approximate strain rate of $2.5 \times 10^{-4}\,s^{-1}$. An image acquisition system including a telecentric lens with the field of view of 3×3 $mm^2$ mounted on a 1'000 × 1'000 pixels digital camera (Pike, Allied Vision, Exton, USA) was used for gathering pictures from the gauge length of the specimens during the tensile experiments. Examination showed that the surface roughness of the strut samples creates enough contrast for image analysis and no speckling was required. An in-house developed Python script based on Lucas-Kanade optical flow tracker was used for analysing the corresponding images and calculating strain evolution during the tensile experiments for strut samples [39].

Mechanical response characterization of the lattice specimens was performed using a 100 kN universal servohydraulic walter + bai machine (walter + bai Testing Machines, Löhningen, Switzerland), Fig. 3b. A side entry extensometer (Epsilon Technology Corp, Jackson, USA) with the gauge length of 15 mm was employed for monitoring the deformation response of the testpieces. Similar to that for the miniature-specimens, the tensile tests for lattices were conducted at a cross-head speed equivalent to an approximate nominal strain rate of $2.5 \times 10^{-4}\,s^{-1}$.

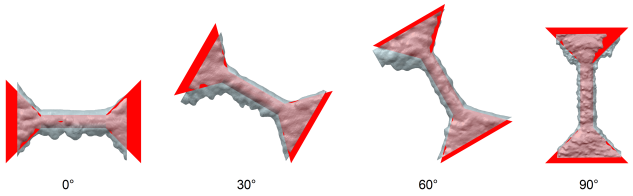


Figure 4: Examples of µCT reconstructed geometries for the miniature tensile specimens with a nominal diameter of 200 µm for different build orientations, including a comparison with their 'nominal' geometries.

### 2.3. Micro-computed tomography

One sample for each diameter-orientation class was chosen for µCT analysis to evaluate the 'true' geometry of the manufactured miniature tensile specimens. The measurements were performed on an RX Solutions EasyTom XL Ultra 230-160 (RX Solutions, Chavanod-Annecy, France) laboratory-based X-ray µCT machine. The system included a Hamamatsu L10801 230 kV microfocus tube with a tungsten target, a beryllium window and a water-cooled tube head. The detector was a 1'920 × 1'536 pixels Varian flat panel with 127 µm pitch and columnar grown CsI as scintillating material. The used acceleration voltage was 100 kV with a nominal current of 150 to 200 µA depending on the object size. The number of projections was 1'440 (over 360°). The commercial software of RX solutions was used for the 3D reconstruction (filtered back projection with 75% sharpness limit, and voxel size of 6 µm). The data is stored in a 16 bit TIFF-format and were subsequently processed using commercial image analysis packages of Mimics Research 21 (Materialise, Leuven, Belgium) and 3-Matic Research 13 (Materialise, Leuven, Belgium). Mimics was used to generate 3D STL models from the µCT TIFF pictures. The 3-Matic employed the 3D STL models to create C3D10 meshes (ten-node tetrahedral elements) with a surface element size of 10 µm to be employed for FE mechanical analysis. Fig. 4 presents examples of the µCT regenerated geometries for the miniature tensile specimens.

### 2.4. Finite element modelling

Finite element (FE) models were developed for analysing the deformation response of the miniature and lattice specimens. FE analysis of the miniature-specimens aimed to consider the µCT data and calculate an equivalent cross-section and accordingly the 'true' stress-strain response of the strut testpieces. The 3D-Matics generated C3D10 meshes for the different diameter-orientation classes of the miniature-specimens were imported into the commercial FE package of Abaqus 2020 (Simulia, Providence, RI). A fictitious elastic-ideally-plastic material with the elastic modulus of 100 GPa and elastic limit

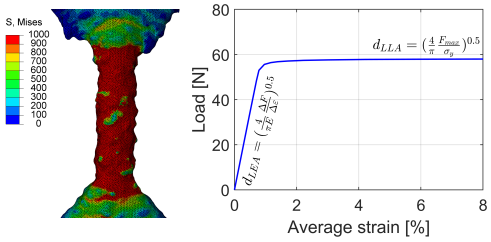


Figure 5: Example of FE simulation results for calculating the 'true' equivalent-diameters of miniature tensile specimens based on linear elastic and limit load analyses.

of 1000 MPa was assigned to the specimens. Abaqus implicit solver was used to simulate the deformation response of the miniature-specimens up to 8 % axial nominal tensile strain. As shown in Fig. 5, the obtained force-strain curves showed an initial linear segment and a final plateau at the maximum force. The observed slope of the linear segment ($\frac{\Delta F}{\Delta \varepsilon}$) and the maximum force ($F_{max}$) can be used for calculating equivalent diameters of the true geometry, based on their linear elastic response and limit load analyses [40], i.e. $d_{LEA}$ and $d_{LLA}$, respectively:

$$E_f = \frac{\Delta\sigma}{\Delta\varepsilon} = \frac{\Delta F}{\pi\left(\frac{d_{LEA}}{2}\right)^2}\frac{1}{\Delta\varepsilon} \rightarrow d_{LEA} = \left(\frac{4}{\pi E_f}\frac{\Delta F}{\Delta\varepsilon}\right)^{0.5} \quad (1)$$

$$F_{max} = \sigma_{0,f}\pi\left(\frac{d_{LLA}}{2}\right)^2 \rightarrow d_{LLA} = \left(\frac{4}{\pi}\frac{F_{max}}{\sigma_{0,f}}\right)^{0.5} \quad (2)$$

where $E_f$ and $\sigma_{0,f}$ are the fictitious elastic modulus and elastic limit (100 GPa and 1000 MPa), respectively. Along with the 'nominal' diameters, the 'true' equivalent-diameters were employed to interpret the experimental observations from the miniature tensile experiments and discuss the size- and orientation-dependence of their constitutive stress-strain response.

The ultimate application of the developed constitutive models would be in mechanical analyses required for the design and topology optimization of lattice structures. Therefore it is essential to evaluate the relevance of employing the developed constitutive models for representing the deformation response of lattice structures. An Abaqus FE model was therefore developed considering the 'nominal' geometry of lattice samples, presented in Fig 2, and the apparent constitutive responses of the 200 µm-thick struts. The designed FE model took advantage of the symmetry by only analysing one-eighth of the geometry and had 1.2 million C3D10 elements (element size of ≥ 50 µm). The FE analysis took 3.4 h using eight threads of Intel Xeon E5-2680v3 processor and required 50 GB memory. Reducing the element size by a factor of two significantly increased the memory requirement and computational time, while the predicted forces by the implicit solver were varied by less than one percent, confirming the reliability of the results. The model's boundary conditions were consistent with the conducted experiments, described in Sec. 2.2. Ultimately, the calculated axial force and displacement at the extensometer location were extracted to be compared with the experimental observations.

Efforts were also made to adopt the 'true' constitutive models and construct an FE model based on the µCT reconstructed lattice geometry and evaluate the benefit of considering a more realistic material model and geometry for representing the deformation response of lattices. This however required adoption of very small elements to capture the topological irregularities of the 'true' topology of lattices and therefore the computational cost increased to unaffordable scales. This approach was therefore abandoned.

## 3. Experimental results

This section first presents the experimental observations from the miniature-specimen tensile tests and derives the apparent stress-strain responses for different diameter-orientation classes of LPBF Ti6Al4V samples. Next, the µCT data are presented to discuss the size- and orientation-dependence of 'geometrical mismatch' and the corresponding 'true' tensile response of the LPBF Ti6Al4V thin struts. Finally, the experimental records for the tensile response of lattice samples with a 'nominal' strut diameter of 200 µm are presented.

### 3.1. Raw data of miniature tensile experiments

Fig. 6 presents the experimentally measured force-strain response of the miniature Ti6Al4V specimens manufactured through LPBF for different build orientations and diameters. Supplementary Materials provides a MATLAB® database including the raw data of the conducted experiments. For each specimen's diameter-orientation class, the results of six tests have been presented to provide an overview of the samples' mechanical response variability. It can be seen that the variability in the mechanical response of samples printed vertically and with diameters larger than 200 µm is low. On the other hand, the tensile test results from horizontal samples show a significant level of variability, which increases with a decrease in the sample diameter. It is known that repeatable and accurate manufacturing of geometrical features aligning horizontal and/or with sub-milimeter dimensions is challenging through LPBF. The observations on the dependency of the variability of the tensile test results to the size and build orientation of miniature samples can therefore be attributed to the inferior control of the LPBF process for the deposition of thin or horizontally-aligned features.

### 3.2. Miniature-specimen apparent tensile response

The 'nominal' diameters of the miniature-specimens were used to calculate their apparent stress-strain curves, presented in Figs. 7-9. A stronger mechanical response for thinner samples was observed, Fig. 7. Furthermore and as can be seen in Fig. 8, the apparent stress-strain curves imply an anisotropic mechanical response, where the strength is typically larger for build orientations of 30° and 60° when compared to 90° and 0°. It is expected that the observed size dependence and the rather uncommon anisotropy are mainly induced by the deviation of true/nominal geometries of the miniature samples (as discussed in the next section).

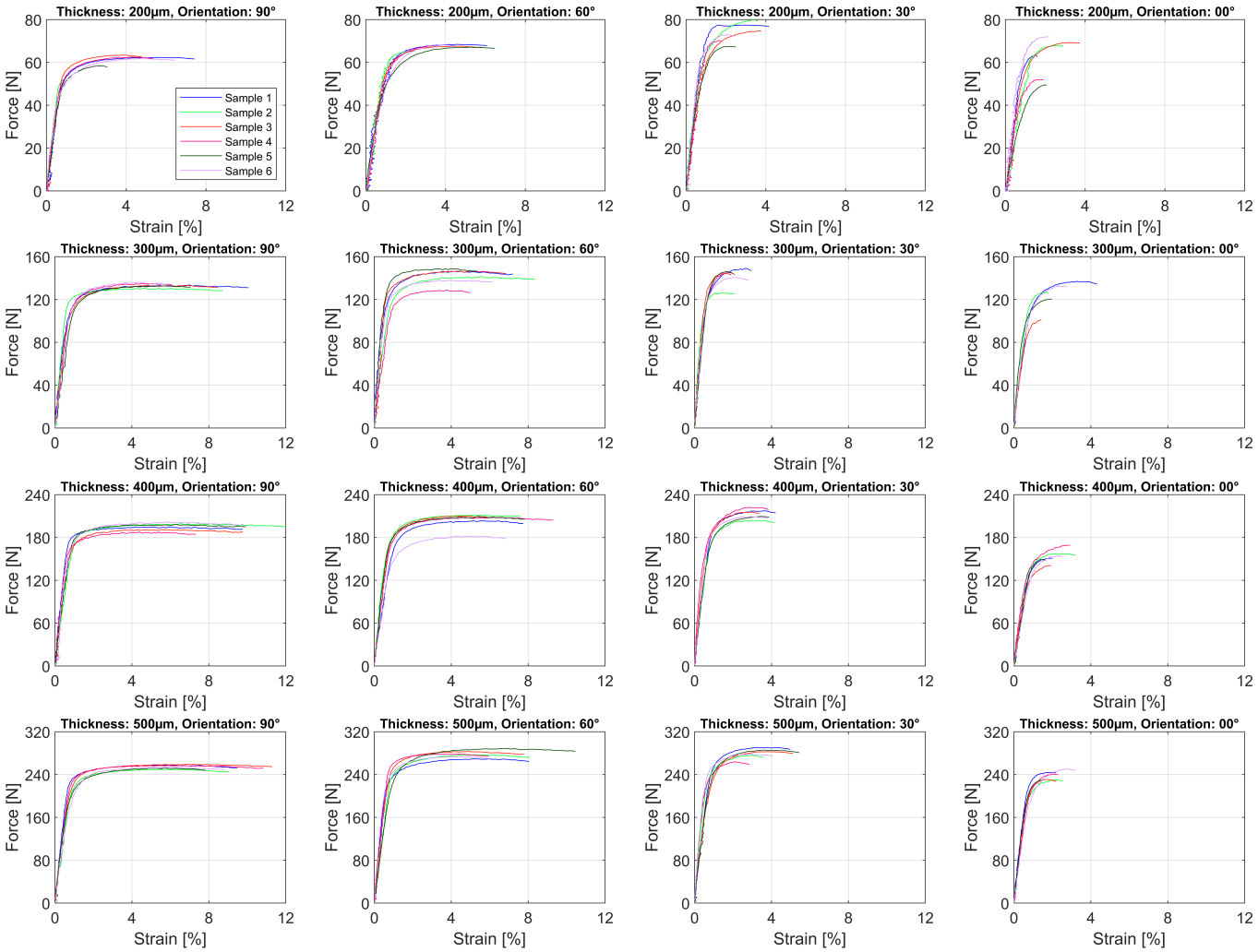


Figure 6: Experimentally measured force-strain response of the miniature LPBF Ti6Al4V samples for different build orientations and diameters.

Fig. 9 presents the derived apparent elastic modules, proof/tensile strengths and ductility of the LPBF miniature specimens for different diameters and build orientations. Importantly, the apparent elastic modulus and strength of the miniature samples are significantly larger than the expected values for Ti6Al4V, e.g. elastic modulus of 113.8 GPa, yield and tensile strength of 880 MPa and 950 MPa, respectively [41, 42]

### 3.3. 'True' diameters of miniature-specimen

The µCT data have been considered in the elastic-plastic FE analysis for determining the 'true' equivalent-diameters of the different classes of miniature samples, see Fig. 5. Table 2 summarizes the corresponding results for $d_{LEA}$ and $d_{LLA}$. Fig. 10 compares the 'geometrical mismatch' of the samples in terms of an oversize factor (i.e. ratio of 'true' to 'nominal' diameters), which indicate that the extent of over-sizing is larger for thinner samples manufactured with build orientations of 0° and 30°.

It should be noted that $d_{LEA}$ is consistently higher than $d_{LLA}$ for all the samples. This is attribute to the fact that the limit load analysis would be more significantly influenced by the notch effects associated with the diameters variations of samples. Nevertheless, the values $d_{LEA}$ and $d_{LLA}$ and consequently the derived oversize factors are quite similar for most samples and therefore calculation of the 'true' stress-strain curves in the next section used the average of the calculated quantities, i.e. $d_{true} = 0.5 \times (d_{LEA} + d_{LLA})$.

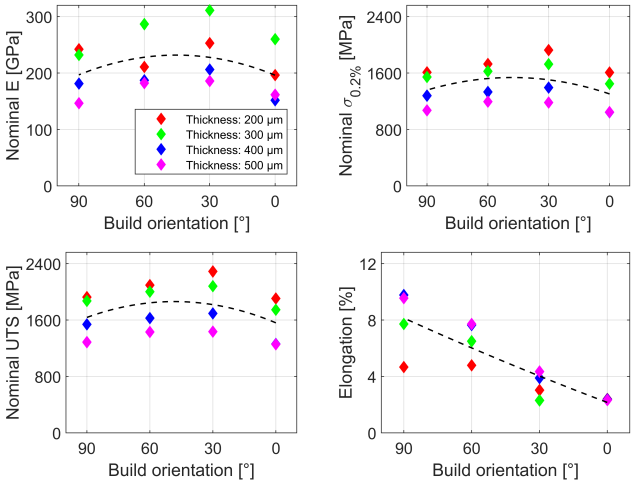


Figure 9: Apparent elastic modulus, 0.2 % proof strength, ultimate tensile strength and elongation of LPBF Ti6Al4V miniature-specimens.

Table 2: Calculated $d_{LEA}$, $d_{LLA}$, $d_{true}$, and oversize extent for the LPBF Ti6Al4V miniature tensile specimens.

| $d_{nom}$ µm | $\alpha$ ° | $d_{LEA}$ µm | $d_{LLA}$ µm | $d_{true}$ µm | Oversize - |
|---|---|---|---|---|---|
| 200 | 90 | 296 | 272 | 284 | 42 |
| 200 | 60 | 301 | 277 | 289 | 45 |
| 200 | 30 | 312 | 301 | 307 | 53 |
| 200 | 0 | 312 | 297 | 305 | 52 |
| 300 | 90 | 393 | 392 | 393 | 31 |
| 300 | 60 | 426 | 407 | 417 | 39 |
| 300 | 30 | 432 | 417 | 425 | 42 |
| 300 | 0 | 391 | 381 | 386 | 29 |
| 400 | 90 | 474 | 471 | 473 | 18 |
| 400 | 60 | 491 | 486 | 489 | 22 |
| 400 | 30 | 528 | 506 | 517 | 29 |
| 400 | 0 | 494 | 488 | 491 | 23 |
| 500 | 90 | 541 | 539 | 540 | 8 |
| 500 | 60 | 607 | 577 | 592 | 18 |
| 500 | 30 | 590 | 580 | 585 | 17 |
| 500 | 0 | 560 | 552 | 556 | 11 |

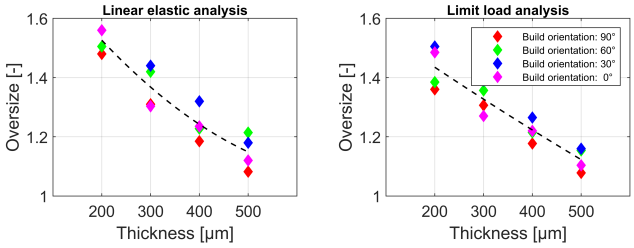


Figure 10: Derived geometrical oversize factors for the LPBF manufactured Ti6Al4V miniature samples. The presented results originate from assessing the µCT data based on a) linear elastic, and b) limit load analyses.

### 3.4. Miniature-specimen 'true' tensile response

Figs. 11 - 13 illustrate the calculated 'true' tensile response for the LPBF miniature Ti6Al4V samples. Compared with the apparent stress-strain curves, a considerably less pronounced dependence on the diameter and build orientation was observed for the 'true' stress-strain curves. Therefore, it can be concluded that the anisotropy and geometry (size) dependence of the apparent stress-strain response of miniature samples mainly arose from the size and orientation dependence of their 'oversize' factor. Although it was not possible to derive consistent dependency trends for the 'true' stress-strain response with respect to the diameter and build orientation, it could be often observed that thicker samples built vertically exhibited stronger mechanical response. . It should be acknowledged that the derivation of the 'true' tensile response here did not account for the effects of the sub-surface irregularities (e.g. pores) which might exist in the strut samples.

In contrast to observations here, previous studies often reported a significant anisotropy in the tensile response of LPBF Ti6Al4V [43, 44]. Their observations were explained based on directional solidification and epitaxial growth during the LPBF process which result in the formation of strong crystallographic textures. As reported by Leicht et al. [45, 46] for AISI 316L, the contribution of epitaxial growth and directional solidification reduces for depositing thin structures and therefore a rather ran-

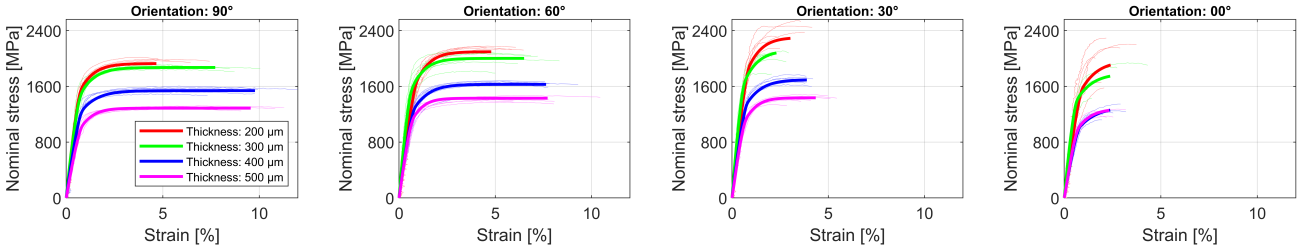


Figure 7: Size dependence of apparent stress-strain response of LPBF Ti6Al4V with different diameters (bold curves: model, shaded curves: experimental).

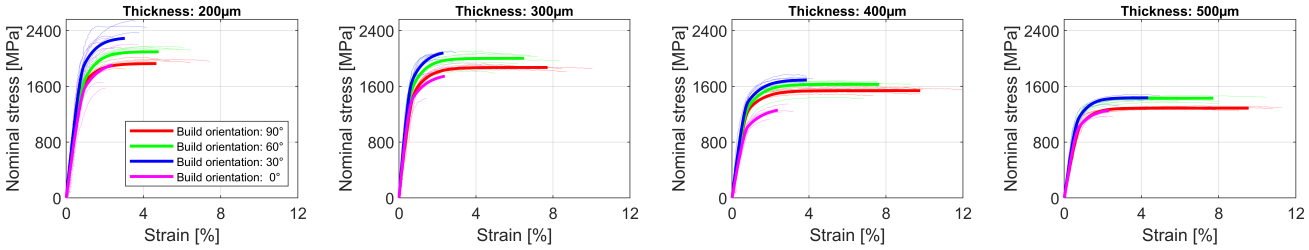


Figure 8: Orientation dependence of apparent stress-strain response of LPBF Ti6Al4V with different built orientations (bold curves: model, shaded curves: experimental).

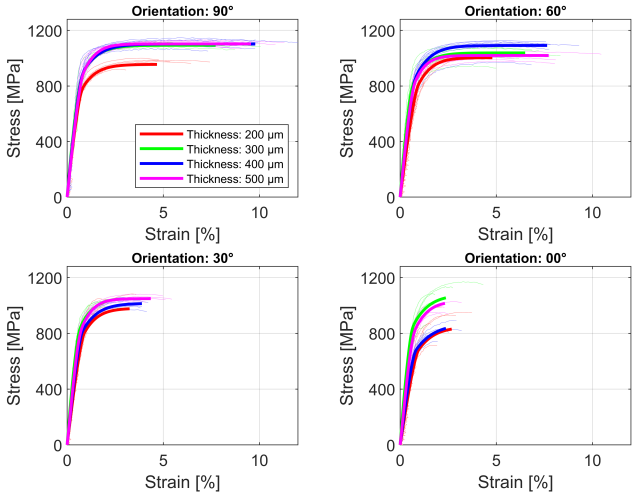


Figure 11: Size dependence of 'true' stress-strain response of LPBF Ti6Al4V with different built orientations (bold curves: model, shaded curves: experimental).

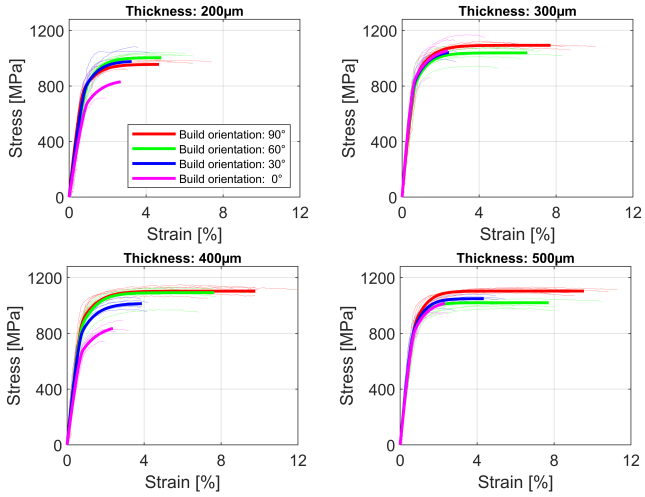


Figure 12: Orientation dependence of 'true' stress-strain response of LPBF Ti6Al4V with different diameters (bold curves: model, shaded curves: experimental).

dom texture is expected for the manufactured miniature samples in this study hence explaining the observed week anisotropy in their 'true' tensile response.

### *3.5. Lattice tensile response*

Fig. 14a presents the experimental observations for the tensile response of lattice specimens with nominal strut diameter of 200 µm. In contrast to the observations for the miniature-specimens, the lattices did not show significant specimen-to-specimen variability in their tensile responses. Fracture occurred in the middle of the samples, perpendicular or at an angle of 45° to the axial loading direction. Scanning electron microscopy (SEM) analysis of the fracture surface of the samples, Fig. 14b, indicated a transgranular ductile fracture mode.

The following section determines constitutive material models for the different diameter-orientation classes of miniature-specimens. The models developed for 200 µm thick samples will be used for predicting the mechanical response of the lattice samples.

## 4. Constitutive material model

For the description of the stress–strain behaviour, it is typically assumed that the increment of total strain tensor ($d\boldsymbol{\varepsilon}$) can additively be decomposed into elastic ($d\boldsymbol{\varepsilon}_{el}$) and plastic ($d\boldsymbol{\varepsilon}_{pl}$)

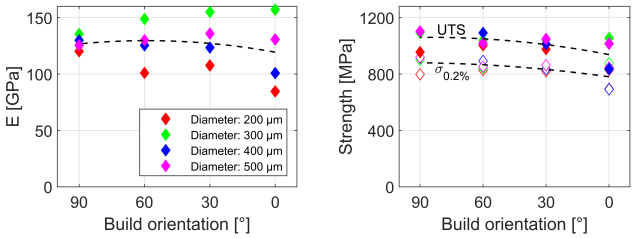


Figure 13: 'True' elastic modulus, 0.2 % proof strength and ultimate tensile strength of LPBF Ti6Al4V miniature-specimens.

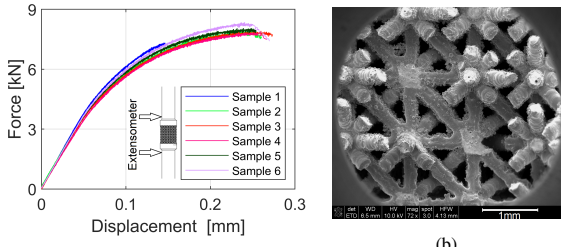


(a) (b)

Figure 14: a) Experimentally observed force-displacement response of LPBF Ti6Al4V lattice specimens (inset: extensometer arrangement for measuring displacement, see Fig. 3), b) SEM image illustrating the fracture surface of a lattice specimen.

components:

$$d\boldsymbol{\varepsilon} = d\boldsymbol{\varepsilon}_{el} + d\boldsymbol{\varepsilon}_{pl} \tag{3}$$

Based on Hook's law, the elastic contribution is simply the increment of the stress tensor ($d\boldsymbol{\sigma}$) multiplied by the compliance tensor ($S$), i.e. inverse of elastic modulus for 1D.

$$d\boldsymbol{\varepsilon}_{el} = \boldsymbol{S}\, d\boldsymbol{\sigma} \tag{4}$$

Assuming a yield potential function ($f$), the increment of the plastic strain tensor can be defined as:

$$d\boldsymbol{\varepsilon}_{pl} = d\lambda \frac{df}{d\boldsymbol{\sigma}} \tag{5}$$

The direction of the plastic strain increment is normal to the yield potential function ($\frac{df}{d\boldsymbol{\sigma}}$) and its extent ($d\lambda$) is derived based on the consistency condition:

$$df = \frac{\partial f}{\partial \boldsymbol{\sigma}} d\boldsymbol{\sigma} + \frac{\partial f}{\partial \boldsymbol{\varepsilon}_{pl}} d\boldsymbol{\varepsilon}_{pl} = 0 \tag{6}$$

The von Mises yield potential function is used here:

$$f = \left[\frac{3}{2}\boldsymbol{\sigma} : \boldsymbol{\sigma}\right]^{\frac{1}{2}} - (\sigma_0 + K) = 0 \tag{7}$$

where $\sigma_0$ is the elastic limit (yield stress) and $K$ is the drag stress, accounting for the (isotropic) strain hardening response of materials. The increase of drag stress and expansion of the yield potential surface was assumed to follow a variant of Voce's non-linear hardening model [47]:

$$K = \sum_{i=1}^{2} Q_i \left(1 - \exp\left(-b_i \bar{\varepsilon}_{pl}\right)\right) \tag{8}$$

Table 3: Material model parameters for representing the apparent and ['true'] stress-strain responses of LPBF Ti6Al4V miniature samples.

| Sample Dia. µm | Angle ° | $E$ GPa | $\sigma_0$ MPa | $Q_1$ MPa | $b_1$ - | $Q_2$ MPa | $b_2$ - |
|---|---|---|---|---|---|---|---|
| 200 | 90 | 273 [135] | 59 [30] | 1382 [685] | 2002 | 486 [241] | 161 |
| 200 | 60 | 224 [107] | 90 [43] | 1437 [688] | 2613 | 570 [273] | 179 |
| 200 | 30 | 261 [111] | 91 [39] | 1653 [704] | 3019 | 558 [238] | 176 |
| 200 | 0 | 200 [ 86] | 62 [27] | 1412 [609] | 3195 | 488 [210] | 150 |
| 300 | 90 | 288 [168] | 43 [25] | 1309 [765] | 1433 | 519 [303] | 151 |
| 300 | 60 | 344 [178] | 65 [33] | 1328 [689] | 1874 | 609 [316] | 168 |
| 300 | 30 | 355 [177] | 65 [33] | 1453 [726] | 2166 | 596 [298] | 165 |
| 300 | 0 | 293 [177] | 45 [27] | 1257 [760] | 2301 | 484 [292] | 140 |
| 400 | 90 | 206 [148] | 42 [30] | 1120 [802] | 1877 | 377 [270] | 139 |
| 400 | 60 | 204 [137] | 64 [43] | 1124 [754] | 2454 | 440 [295] | 154 |
| 400 | 30 | 219 [131] | 65 [39] | 1200 [718] | 2834 | 432 [259] | 151 |
| 400 | 0 | 158 [105] | 44 [30] | 911 [605] | 3013 | 349 [232] | 129 |
| 500 | 90 | 157 [135] | 43 [37] | 897 [769] | 2484 | 347 [298] | 194 |
| 500 | 60 | 187 [134] | 65 [46] | 990 [706] | 3644 | 375 [268] | 217 |
| 500 | 30 | 186 [136] | 65 [48] | 981 [716] | 4215 | 389 [284] | 212 |
| 500 | 0 | 158 [128] | 45 [36] | 908 [735] | 4485 | 323 [261] | 181 |

Superposition of two exponential terms was used to represent the hardening response of the material during the initial and later plastification. Quantities $Q_i$ and $b_i$ are the maximum contribution and rate of strain-hardening for each term, and $\bar{\varepsilon}_{pl}$ is the accumulated von Mises plastic strain. It should be noted that the above model is a rather simple variant of the Chaboche constitutive model [48, 49] with two nonlinear isotropic hardening terms [50] and therefore its application is limited for representing materials behaviour for small to moderate extent of monotonic deformation.

The above formulations describe materials' elastic and isotropic-hardening plasticity response based on seven materials parameter; $E$, $\nu$, $\sigma_0$, $Q_{1-2}$, and $b_{1-2}$. A Poisson's ratio of $\nu = 0.34$ is considered for Ti6Al4V [41]. The derived 'apparent' and 'true' stress-strain curves were exploited to determine the other six material parameters for each diameter-orientation class of miniature samples through a least-squares regression optimization, considering their six repeat-tests.

Table 3 summaries the derived model parameters for each diameter-orientation class of miniature samples. Figs. 7 – 12 compare the model representations against the experimentally derived 'apparent' and 'true' stress-strain curves which demonstrate the effectiveness of the presented constitutive material model. As the ultimate application of the developed constitutive models is for mechanical analyses of lattice structures, it is essential to evaluate them for representing the deformation response of lattices. The followings will therefore examine the predictive ability of the apparent constitutive models in the FE model, representing the 'nominal' geometry of lattices

## 5. FE simulation of lattices

The developed apparent constitutive material models for miniature-specimens manufactured with the nominal diameter of 200 µm were implemented into FE model for simulating the tensile response of lattices with the strut diameter of 200 µm. The examined tetrahedron lattice includes struts oriented 0°,

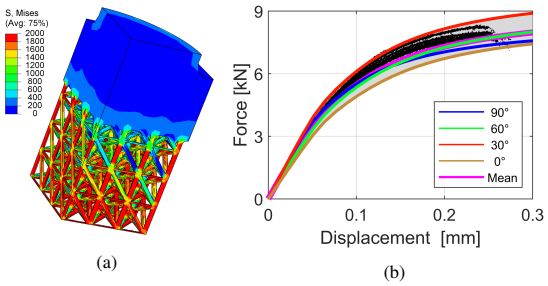


Figure 15: a) An example of FE calculated distribution of stresses within the lattice specimen. b) comparison of FE predictions vs experimental observations for the tensile response of the lattices.

45°, 54.74° and 90° with respect to the built orientation. This study performed four sets of FE simulations employing apparent constitutive models for build orientations of 0°, 30°, 60° and 90° and analysed the results to derive upper and lower bounds as well as average deformation response of the lattice samples. Comparison of the experimental force-displacement responses with those predicted by the FE models in Fig. 15 indicates that the consideration of the apparent constitutive material models in the FE analysis provides an acceptable approximation of the experimentally observed tensile response of the lattices. The FE predictions resulted from consideration of the 60° apparent constitutive model gave the closest representation for the experimental data which can be attributed to the fact that the highly loaded struts within the lattice are 45°, 54.74° and 90° oriented which are, on average, close to the deposition orientation of 60°.

Employment of the 'true' constitutive material models into an FE model constructed based on μCT geometrical data is expected to provide a more reliable representation of the lattices' mechanical response. However, such a FE model needs very small elements (e.g. <10 μm) to enable capturing the irregularities of the 'true' topology of lattices and consequently demands unrealistically high computational memory. Furthermore, employment of μCT reconstructed geometries for FE analysis of lattice-based implants is not practical. Particularly, information regarding the 'true' geometry of lattices is not accessible at the design stage, and therefore employment of the 'true' constitutive models for the design and topology optimization analyses of lattice-based implants is not feasible. As an alternative, this study showed that consideration of apparent constitutive models in FE models with the nominal geometry of lattices might be considered as a useful engineering approximation for such applications.

## 6. Concluding Remarks

The present study reports observations from a comprehensive experimental program examining the mechanical response of Ti6Al4V miniature-specimens built through laser powder bed fusion (LPBF) process. The examined specimens were manufactured with a range of diameters and build orientations. Examining the apparent stress-strain behaviour of the samples (based on their 'nominal' diameters) indicated a stronger response for the thinner samples built under the orientations of 30° and 60°. Importantly, the calculated apparent elastic moduli and strengths were significantly larger than the expected values for Ti6Al4V. Observations from the micro-computed tomography (μCT) were employed for determining the 'true' geometry of the built samples, which revealed that the 'true' diameters of the samples were significantly larger than the 'nominal' ones, in particular for thinner samples manufactured under build orientations of 0° and 30°. A less pronounced dependence on diameter and build orientation was observed for the 'true' stress-strain curves. Therefore, it can be concluded that the anisotropy and size dependence of the apparent stress-strain response of miniature samples mainly arose from the size and orientation dependence of their 'geometrical mismatch'.

Material constitutive models were developed to represent the 'apparent' and 'true' deformation response of the different diameter-orientation classes of the miniature samples. The derived apparent constitutive models for samples with the diameter of 200 μm were implemented for numerical calculation of the tensile response of lattice samples with a nominal strut diameter of 200 μm. Consideration of the apparent constitutive models in FE analyses (based on the nominal geometry of lattices) could provide reliable deformation response predictions at a reasonable computing cost. On the other hand considering the 'true' mechanical response of struts in the design and topology optimization analyses of lattice-based implants is not practically feasible, since it leads to enormous computational costs and it would require information regarding the 'true' geometry of lattices that is not accessible at the design stage. As an alternative, the present analysis indicates that consideration of the apparent constitutive response of the struts in FE models representing the nominal geometry of lattices provides acceptable approximations for their experimentally observed deformation response and, therefore might be employed for design analysis and topology optimization of such lattice structures. It is however evident that the predicted stress values by such a simulation strategy are a significant overestimation of the 'true' stresses and cannot be further interpreted or exploited e.g. for stress-based life assessments. Furthermore, the developed models are rather simple variants of the Chaboche constitutive model with two nonlinear isotropic hardening terms and therefore their application is limited to representing materials' behaviour for small to moderate extent of monotonic deformation

## Acknowledgments

The authors gratefully acknowledge the support of Prof Damiano Pasini (McGill University, Canada) for providing the CAD model for the lattice and his helpful advice and support. The support of Mr. Freddy Bürki for designing the miniature-specimen mechanical testing setup, Dr. Raoul Hopf for providing his Python script for strain analysis, and Mr Daniele Ghedalia for his contribution to the miniature-specimen testing are highly appreciated. The authors also thank Additive De-

sign in Surgical Solutions Center Inc., Canada (ADEISS) for the manufacture of the testpieces.

## Supplementary Materials

A MATLAB® database including the data from the performed tensile experiments for miniature and lattice samples is provided.

## References


[1] Trina Majumdar, Neil Eisenstein, Jess E Frith, Sophie C Cox, and Nick Birbilis. Additive manufacturing of titanium alloys for orthopedic applications: a materials science viewpoint. *Advanced Engineering Materials*, 20(9):1800172, 2018.

[2] Venkata P Mantripragada, Beata Lecka-Czernik, Nabil A Ebraheim, and Ambalangodage C Jayasuriya. An overview of recent advances in designing orthopedic and craniofacial implants. *Journal of biomedical materials research Part A*, 101(11):3349–3364, 2013.

[3] Narges Shayesteh Moghaddam, Mohsen Taheri Andani, Amirhesam Amerinatanzi, Christoph Haberland, Scott Huff, Michael Miller, Mohammad Elahinia, and David Dean. Metals for bone implants: Safety, design, and efficacy. *Biomanufacturing Reviews*, 1(1):1–16, 2016.

[4] Mitsuo Niinomi. Recent metallic materials for biomedical applications. *Metallurgical and materials transactions A*, 33(3):477–486, 2002.

[5] Dan Wu, Per Isaksson, Stephen J Ferguson, and Cecilia Persson. Young's modulus of trabecular bone at the tissue level: A review. *Acta biomaterialia*, 78:1–12, 2018.

[6] Jae Young Rho, Richard B Ashman, and Charles H Turner. Young's modulus of trabecular and cortical bone material: ultrasonic and microtensile measurements. *Journal of biomechanics*, 26(2):111–119, 1993.

[7] Simon Bernard, Quentin Grimal, and Pascal Laugier. Accurate measurement of cortical bone elasticity tensor with resonant ultrasound spectroscopy. *Journal of the mechanical behavior of biomedical materials*, 18:12–19, 2013.

[8] Charles H Turner, Jae Rho, Yuichi Takano, Ting Y Tsui, and George M Pharr. The elastic properties of trabecular and cortical bone tissues are similar: results from two microscopic measurement techniques. *Journal of biomechanics*, 32(4):437–441, 1999.

[9] Theofilos Karachalios, Christos Tsatsaronis, George Efraimis, Panagiotis Papadelis, George Lyritis, and George Diakoumopoulos. The long-term clinical relevance of calcar atrophy caused by stress shielding in total hip arthroplasty: a 10-year, prospective, randomized study. *The Journal of arthroplasty*, 19(4):469–475, 2004.

[10] M Niinomi and M Nakai. Titanium-based biomaterials for preventing stress shielding between implant devices and bone. *International journal of biomaterials*, 2011, 2011.

[11] DR Sumner. Long-term implant fixation and stress-shielding in total hip replacement. *Journal of Biomechanics*, 48(5):797–800, 2015.

[12] D Barba, E Alabort, and RC Reed. Synthetic bone: Design by additive manufacturing. *Acta biomaterialia*, 97:637–656, 2019.

[13] Daniel A Shimko, Valerie Franz Shimko, Edward A Sander, Kyle F Dickson, and Eric A Nauman. Effect of porosity on the fluid flow characteristics and mechanical properties of tantalum scaffolds. *Journal of Biomedical Materials Research Part B: Applied Biomaterials: An Official Journal of The Society for Biomaterials, The Japanese Society for Biomaterials, and The Australian Society for Biomaterials and the Korean Society for Biomaterials*, 73(2):315–324, 2005.

[14] Krzysztof Pałka and Rafał Pokrowiecki. Porous titanium implants: a review. *Advanced Engineering Materials*, 20(5):1700648, 2018.

[15] AP Rubshtein, I Sh Trakhtenberg, EB Makarova, EB Triphonova, DG Bliznets, LI Yakovenkova, and AB Vladimirov. Porous material based on spongy titanium granules: structure, mechanical properties, and osseointegration. *Materials Science and Engineering: C*, 35:363–369, 2014.

[16] Peter Jordan Kwok, Scott M Oppenheimer, and David C Dunand. Porous titanium by electro-chemical dissolution of steel space-holders. *Advanced engineering materials*, 10(9):820–825, 2008.

[17] Lenko Stanev, Mihail Kolev, Boris Drenchev, and Ludmil Drenchev. Open-cell metallic porous materials obtained through space holders—part i: Production methods. a review. *Journal of Manufacturing Science and Engineering*, 139(5), 2017.

[18] Zhonghan Wang, Chenyu Wang, Chen Li, Yanguo Qin, Lei Zhong, Bingpeng Chen, Zhaoyan Li, He Liu, Fei Chang, and Jincheng Wang. Analysis of factors influencing bone ingrowth into three-dimensional printed porous metal scaffolds: a review. *Journal of Alloys and Compounds*, 717:271–285, 2017.

[19] Mitsuru Takemoto, Shunshuke Fujibayashi, Mashashi Neo, Jun Suzuki, Tadashi Kokubo, and Takashi Nakamura. Mechanical properties and osteoconductivity of porous bioactive titanium. *Biomaterials*, 26(30):6014–6023, 2005.

[20] D Melancon, ZS Bagheri, RB Johnston, L Liu, M Tanzer, and D Pasini. Mechanical characterization of structurally porous biomaterials built via additive manufacturing: experiments, predictive models, and design maps for load-bearing bone replacement implants. *Acta biomaterialia*, 63:350–368, 2017.

[21] Yingjun Wang, Sajad Arabnejad, Michael Tanzer, and Damiano Pasini. Hip implant design with three-dimensional porous architecture of optimized graded density. *Journal of Mechanical Design*, 140(11), 2018.

[22] Amir A Zadpoor. Additively manufactured porous metallic biomaterials. *Journal of Materials Chemistry B*, 7(26):4088–4117, 2019.

[23] XZ Zhang, M Leary, HP Tang, T Song, and M Qian. Selective electron beam manufactured ti-6al-4v lattice structures for orthopedic implant applications: Current status and outstanding challenges. *Current Opinion in Solid State and Materials Science*, 22(3):75–99, 2018.

[24] S Murchio, M Dallago, F Zanini, S Carmignato, G Zappini, F Berto, D Maniglio, and M Benedetti. Additively manufactured ti–6al–4v thin struts via laser powder bed fusion: Effect of building orientation on geometrical accuracy and mechanical properties. *Journal of the Mechanical Behavior of Biomedical Materials*, 119:104495, 2021.

[25] Xiaojian Wang, Shanqing Xu, Shiwei Zhou, Wei Xu, Martin Leary, Peter Choong, Ma Qian, Milan Brandt, and Yi Min Xie. Topological design and additive manufacturing of porous metals for bone scaffolds and orthopaedic implants: A review. *Biomaterials*, 83:127–141, 2016.

[26] Elena Provaggi, Julian JH Leong, and Deepak M Kalaskar. Applications of 3d printing in the management of severe spinal conditions. *Proceedings of the Institution of Mechanical Engineers, Part H: Journal of Engineering in Medicine*, 231(6):471–486, 2017.

[27] Sajad Arabnejad, R Burnett Johnston, Jenny Ann Pura, Baljinder Singh, Michael Tanzer, and Damiano Pasini. High-strength porous biomaterials for bone replacement: A strategy to assess the interplay between cell morphology, mechanical properties, bone ingrowth and manufacturing constraints. *Acta biomaterialia*, 30:345–356, 2016.

[28] FSL Bobbert and AA Zadpoor. Effects of bone substitute architecture and surface properties on cell response, angiogenesis, and structure of new bone. *Journal of Materials Chemistry B*, 5(31):6175–6192, 2017.

[29] John J Lewandowski and Mohsen Seifi. Metal additive manufacturing: A review of mechanical properties (postprint). 2016.

[30] Daniel Greitemeier, Claudio Dalle Donne, Achim Schoberth, Michael Jürgens, Jens Eufinger, and Tobias Melz. Uncertainty of additive manufactured ti-6al-4v: chemistry, microstructure and mechanical properties. In *Applied Mechanics and Materials*, volume 807, pages 169–180. Trans Tech Publ, 2015.

[31] Stéphane Gorsse, Christopher Hutchinson, Mohamed Gouné, and Rajarshi Banerjee. Additive manufacturing of metals: a brief review of the characteristic microstructures and properties of steels, ti-6al-4v and high-entropy alloys. *Science and Technology of advanced MaTerialS*, 18(1):584–610, 2017.

[32] Harry Bikas, Panagiotis Stavropoulos, and George Chryssolouris. Additive manufacturing methods and modelling approaches: a critical review. *The International Journal of Advanced Manufacturing Technology*, 83(1):389–405, 2016.

[33] Dalia Mahmoud and Mohamed A Elbestawi. Lattice structures and functionally graded materials applications in additive manufacturing of orthopedic implants: a review. *Journal of Manufacturing and Materials Processing*, 1(2):13, 2017.

[34] A Pérez-Sánchez, A Yánez, A Cuadrado, O Martel, and N Nuño. Fatigue behaviour and equivalent diameter of single ti-6al-4v struts fabricated by electron bean melting orientated to porous lattice structures. *Materials &*

*Design*, 155:106–115, 2018.

[35] Eren Pehlivan, Michaela Roudnicka, Jan Dzugan, Martina Koukolikova, Vlastimil Králík, Mohsen Seifi, John J Lewandowski, Dalibor Dalibor, and Matej Daniel. Effects of build orientation and sample geometry on the mechanical response of miniature cp-ti grade 2 strut samples manufactured by laser powder bed fusion. *Additive Manufacturing*, 35:101403, 2020.

[36] Volker Weißmann, Philipp Drescher, Rainer Bader, Hermann Seitz, Harald Hansmann, and Nico Laufer. Comparison of single ti6al4v struts made using selective laser melting and electron beam melting subject to part orientation. *Metals*, 7(3):91, 2017.

[37] JL Grenestedt. On interactions between imperfections in cellular solids. *Journal of materials science*, 40(22):5853–5857, 2005.

[38] Zahra S Bagheri, David Melancon, Lu Liu, R Burnett Johnston, and Damiano Pasini. Compensation strategy to reduce geometry and mechanics mismatches in porous biomaterials built with selective laser melting. *Journal of the mechanical behavior of biomedical materials*, 70:17–27, 2017.

[39] R. Hopf, L. Bernardi, J. Menze, M. Zündel, E. Mazza, and A. E. Ehret. Experimental and theoretical analyses of the age-dependent large-strain behavior of sylgard 184 (10:1) silicone elastomer. *Journal of the Mechanical Behavior of Biomedical Materials*, 60:425–437, 2016.

[40] Peng-fei Liu, Jin-yang Zheng, Li Ma, Cun-jian Miao, and Lin-lin Wu. Calculations of plastic collapse load of pressure vessel using fea. *Journal of Zhejiang University-SCIENCE A*, 9(7):900–906, 2008.

[41] Metals Handbook. Vol. 2. *Properties and Selection: Nonferrous Alloys and Special-Purpose Materials*, 713, 1990.

[42] ASM. Aerospace Specification Metals INC, Titanium Technical Data. *Titanium Ti-6Al-4V (Grade 5), Annealed*.

[43] Manikandakumar Shunmugavel, Ashwin Polishetty, and Guy Littlefair. Microstructure and mechanical properties of wrought and additive manufactured ti-6al-4 v cylindrical bars. *Procedia Technology*, 20:231–236, 2015.

[44] Wenbo Sun, Yu E Ma, Weihong Zhang, Xudong Qian, Wei Huang, and Zhenhai Wang. Effects of the build direction on mechanical performance of laser powder bed fusion additively manufactured ti6al4v under different loadings. *Advanced Engineering Materials*, 23(12):2100611, 2021.

[45] Alexander Leicht. *Laser powder bed fusion of 316L stainless steel-Microstructure and mechanical properties as a function of process parameters, design and productivity*. PhD thesis, Chalmers Tekniska Hogskola (Sweden), 2020.

[46] Alexander Leicht, Uta Klement, and Eduard Hryha. Effect of build geometry on the microstructural development of 316l parts produced by additive manufacturing. *Materials Characterization*, 143:137–143, 2018.

[47] E Voce. A practical strain hardening function. *Metallurgia*, 51:219–226, 1955.

[48] Jean-Louis Chaboche. Time-independent constitutive theories for cyclic plasticity. *International Journal of plasticity*, 2(2):149–188, 1986.

[49] Jean-Louis Chaboche. Constitutive equations for cyclic plasticity and cyclic viscoplasticity. *International journal of plasticity*, 5(3):247–302, 1989.

[50] Peter J Armstrong, CO Frederick, et al. *A mathematical representation of the multiaxial Bauschinger effect*, volume 731. Berkeley Nuclear Laboratories Berkeley, CA, 1966.